Learning and Predicting Shape Deviations of Smooth and Non-Smooth 3D Geometries Through Mathematical Decomposition of Additive Manufacturing

Yuanxiang Wang, *Member, IEEE*, Cesar Ruiz, and Qiang Huang, *Senior Member, IEEE*

***Abstract*— In additive manufacturing (AM), final product geometries are often deformed or distorted. The deviations of three-dimensional (3D) shapes from their intended designs can be represented as 2D surfaces in a $\mathbb{R}^3$ space, which constitutes a complicated set of data for learning and predicting geometric quality. Patterns of deviation surfaces vary with shape geometries, sizes/volumes, materials, and AM processes. Our previous work has established an engineering-informed convolution framework to learn shape deviation from a small set of training products built with the same material and process. It incorporates the characteristics of the layer-wise shape forming process through a convolution formulation and the size factor for a category of smooth 3D shapes such as domes or cylinders. This study extends this fabrication-aware learning framework to a larger class of products including both smooth and non-smooth surfaces (polyhedral shapes). The key idea of learning heterogeneous deviation surface data under a unified model is to establish the association between the deviation profiles of smooth base shapes and those of non-smooth polyhedral shapes. The association, which is characterized by a novel 3D cookie-cutter function, views polyhedral shapes as being carved out from smooth base shapes. In essence, the AM process of building non-smooth shapes is mathematically decomposed into two steps: additively fabricate smooth base shapes using a convolution learning framework, and then subtract extra materials using a cookie-cutter function. The proposed joint learning framework of shape deviation data reflects this decomposition by adopting a sequential model estimation procedure. The model learning procedure first establishes the convolution model to capture the effects of layer-wise fabrication and sizes, and then estimates the 3D cookie-cutter function to realize geometric differences between smooth and non-smooth shapes. A new Gaussian process model is proposed to consider the spatial correlation among neighboring regions within a 3D shape and across different shapes. The case study demonstrates the feasibility and prospects of prescriptive learning of complex 3D shape deviations in AM and extension to broader engineering surface data.**

Manuscript received 11 March 2022; accepted 2 May 2022. Date of publication 2 June 2022; date of current version 3 July 2023. This article was recommended for publication by Associate Editor K. Zhu and Editor X. Xie upon evaluation of the reviewers' comments. This work was supported in part by the National Science Foundation under Grant NSF CMMI-1901514 and in part by University of Southern California (USC) Pratt & Whitney Institute for Collaborative Engineering Board (PWICE) Projects. *(Corresponding author: Qiang Huang.)*

The authors are with the Daniel J. Epstein Department of Industrial and Systems Engineering, University of Southern California, Los Angeles, CA 90089 USA (e-mail: qiang.huang@usc.edu).

Color versions of one or more figures in this article are available at https://doi.org/10.1109/TASE.2022.3174228.

Digital Object Identifier 10.1109/TASE.2022.3174228

***Note to Practitioners*—Engineering processes such as 3D printing generate complex shape data in the form of 3D point clouds. Qualification and verification of 3D shapes involves modeling and learning of heterogeneous shape deviation data that are affected by both product geometries and process physics. This study develops an engineering-informed, small-sample machine learning methodology to learn and predict deviations of smooth and non-smooth 3D shapes in a unified modeling framework. The fabrication of a non-smooth 3D shape is mathematically decomposed into the smooth base shape formation and shape difference realization. Both process knowledge and shape geometries are captured in the learning framework. It provides a new data analytical tool for shape engineering in additive manufacturing and beyond.**

***Index Terms*— Shape engineering, shape deviation modeling, convolution, process decomposition, Gaussian process, fabrication-aware machine learning.**

I. Introduction

ADDITIVE manufacturing (AM) or three-dimensional (3D) printing enables the direct fabrication of complicated geometries and a wide range of structures using various materials [1]–[3]. Due to materials phase changes and high thermal gradients in the layer-wise fabrication processes, final product geometries are often deformed or distorted [4]–[9]. The deviations of 3D shapes from their intended designs can be represented as 2D surfaces in a $\mathbb{R}^3$ space [10]–[12], which constitutes a complicated set of data for learning and predicting geometric quality. Patterns of deviation surface data vary with shape geometries, sizes/volumes, materials, and the AM processes [13]–[16].

As a motivating example, four domes and three thin walls with half-cylindrical shapes were vertically printed through an AM process using the same material (Fig. 1). After collecting the point cloud data on the product surfaces and comparing with the designs, we present their shape deviations as functional surfaces [9] in the spherical coordinate system (SCS) as shown in Fig. 2. The deviation profiles of the thin walls are quite different from those of the domes. Thin walls present sharp increments in the deviation around the corners/edges while the deviation surfaces of domes are relatively smooth everywhere. Furthermore, the shape deviation profiles and their patterns can vary with the size of the same target shape.

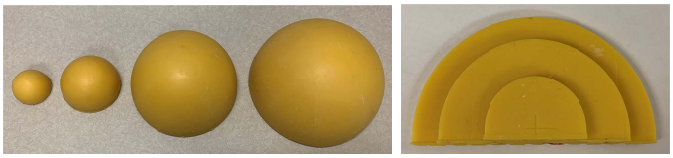

(a) (b)

Fig. 1. (a) Domes with 0.5, 0.8, 1.5 and 1.8 inches radii and (b) thin walls with 0.8, 1.5 and 2.0 inches radii.

To learn and predict surface deviations of 3D shapes, we face several fundamental challenges:

- *Heterogeneity*. Deviation patterns are affected by multiple factors including geometries, sizes, materials and process parameters. This often produces heterogeneous data even under the same process settings of an AM machine. As observed in Fig. 2, thin walls show distinct deviation patterns from domes. Different sizes/volumes would affect not only the magnitude of the deviation surface but also the locations of sharp transitions for the thin walls. Taking the deviation profile as the response, there are three types of covariates: (1) location covariates defined with respect to the printing and registration center [13], [17]; (2) process parameters such as the type of AM process, printing materials, printing temperatures, etc. [12], [18], [19]; and (3) size-and-shape information specified by the designs of AM products [13], [20], [21].
- *Limited samples*. A key advantage of AM is the easy customization of the printed parts. This one-of-a-kind manufacturing approach limits the applicability of large-sample machine learning methods and classical statistical methods for modeling shape deviations. With a limited number of training samples and various covariates, it is challenging to establish a prescriptive model, estimate its parameters, and validate assumptions on model specification and parameters, especially for non-parametric models such as random forest [17] and Dirichlet process [22].
- *Spatial correlation within and among shapes*. In AM, the layer-by-layer fabrication process exacerbates the quality issues related to material phase change and heat penetration observed in traditional manufacturing [23]–[25], leading to stronger spatial correlation among neighboring regions of a product. Joint learning of different 3D shapes presents the additional challenge of defining spatial correlation among different geometries.

In the literature, physics-based and data-driven approaches have been extensively reported to predict printing quality. A common strategy in physics-based modeling is the use of finite element analysis to simulate the printing process and reveal the relationship among process, geometric structure, and material properties [26], [27]. These models can achieve voxel-level accuracy for describing 3D products during the printing process but at a high computational cost. Extensive expert knowledge is required to develop such models and they are typically restricted to a specific material, geometry, and AM process. In the data-driven AM research, regression models [28], [29], design of experiments techniques [30], [31], and machine learning strategies [32], [33] have been applied. However, most data-driven AM models suffer from lack of interpretability and over-fitting issues.

To learn heterogeneous data with limited sample sizes, efforts have been devoted to transfer learning across materials, manufacturing processes, and part designs. Sabbaghi and Huang [18] proposed the effect equivalence framework to calibrate the effects of lurking variables in different AM processes through a base factor, which was adopted by Francis *et al.* [19] to accomplish the model transfer from Ti-6Al-4V to 316L stainless steel. Chen *et al.* [34] achieved knowledge transfer across different shapes by first decomposing the geometric error into shape-independent and shape-specific components and then fixing the global shape-independent parameters and shape features. Ferreira *et al.* [21] employed a Bayesian extreme learning machine methodology to automatically predict the shape deviation profiles of 2D freeform shapes under different printing processes. However, the applicability of these transfer learning methods has not been demonstrated for 3D geometries.

Engineering-informed machine learning approaches have been proposed to model and predict 2D shape deviation using a limited number of training samples. Huang *et al.* [4] developed a prescriptive statistical modeling approach to predict and compensate the 2D shape deviation of circular shapes considering the size effect and lurking variables such as overexposure. It serves as a base model to predict the deviation of circular shapes, regular polygons, and ultimately freeform shapes. A key challenge to model polygonal shapes is that the deviation pattern changes dramatically on the sharp corners due to high residual stresses and thermal gradients [35]. To link the circular shape deviations to those of regular polygons, Huang *et al.* [13] viewed polygons as being mathematically carved out from their circumcircles (base shapes) through cookie-cutter functions. To predict the shape deviation profiles of freeform shapes, Luan and Huang [14] approximated the freeform design with a series of piece-wise circular sectors or polygonal segments.

The modeling and control challenges faced in printing 2D shapes are exacerbated for 3D geometries, since deviation patterns can change from layer to layer due to complex inter-layer interactions, residual stresses and heat dissipation profiles [6], [16]. To incorporate the layer-by-layer fabrication mechanism into modeling and learning, Huang *et al.* [9] proposed a convolution learning framework to describe the 3D deviation patterns as the result of the 2D shape deviation of each layer convolved with a layer interaction function that captures inter-layer interactions. Although this framework was validated with spherical shapes, it still requires fundamental work to predict the complex deviation patterns of both smooth and non-smooth shapes in a consistent unified modeling framework. Due to the smoothing effect of convolution operations, this approach alone is inadequate to capture the sharp transitions in the shape deviation profiles of non-smooth polyhedral geometries such as in thin-wall shapes. The main reason to study these particular shapes is that 3D freeform shapes can be approximated as a combination of smooth and non-smooth patches [36]. Understanding these two basic

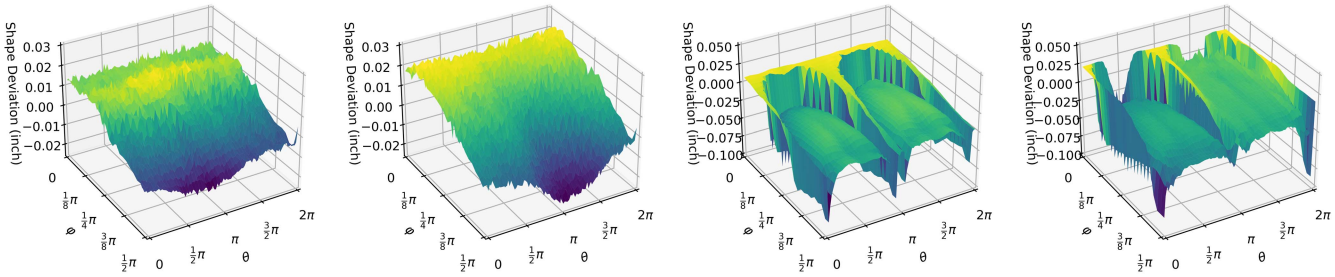

(a) 0.8-inch Dome (b) 1.8-inch Dome (c) 0.8-inch Thin Wall (d) 2.0-inch Thin Wall

Fig. 2. Shape deviation measurements of two dome and two thin walls presented in the SCS (darker purple and lighter yellow color for negative and positive deviation, respectively).

categories of 3D shapes enables 3D freeform shape deviation prediction similar to the significant advances achieved for the 2D case [4], [13], [14].

To tackle these challenges, we mathematically decompose the fabrication of non-smooth 3D shapes into two steps: (1) additively building the smooth base shapes, and (2) subtractively craving out the non-smooth polyhedral shapes. An additive model is proposed to connect smooth and non-smooth 3D geometries through a new 3D cookie-cutter function with an engineering-informed sequentially model estimation strategy. Spatial correlation among regions within a product and across different product geometries is modeled by a Gaussian process (GP) with a novel distance metric integrating both geodesic and geometric information.

The remainder of this paper is organized as follows. Sec. II introduces the model for mathematical decomposition of shape deviation in AM and discusses its components. An engineering-informed sequential model fitting strategy is proposed to enable efficient and stable parameter estimation in Sec. III. Sec. IV demonstrates the proposed framework using printed domes and thin wall shapes. Concluding remarks are given in Sec. V.

II. A Unified Shape Deviation Modeling Approach for Both Smooth and Non-Smooth 3D Geometries in AM

This section proposes a mathematical decomposition of AM as a general additive model to learn and predict shape deviation surfaces of 3D geometries. Adopting smooth shapes as the model baseline, we propose a new class of cookie-cutter functions to link the shape deviations of 3D smooth and non-smooth convex shapes. Lastly, a GP is employed to capture the spatial correlation with a novel distance metric.

A. Mathematical Decomposition of AM Through an Additive Model for Shape Deviation Modeling

To gain insights from the heterogeneous data (Fig. 2), domain knowledge must be incorporated in the modeling framework. As shown in Fig. 3, the process of building a 3D shape can be mathematically decomposed into two steps: (1) additive step, which fabricates a smooth base shape that bounds the target geometry, and (2) subtractive step, which removes extra materials to form non-smooth edges and corners. Thus, the smooth and non-smooth 3D shapes are connected through an association or cookie-cutter function that captures the shape deviation caused by the subtractive step.

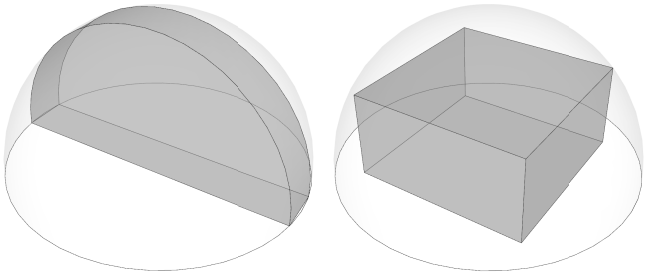

(a) (b)

Fig. 3. Mathematical decomposition of AM to additively build the smooth base shape (outer dome shape) and subtractively carve out non-smooth shapes with sharp corners such as (a) thin wall shape and (b) cuboid shape.

Here, the shape smoothness is defined with respect to the smoothness of curves on the surface of the product design. If any curve along the shape surface is smooth, i.e., there exists a common tangent direction at any point on the surface, then the shape is smooth; otherwise, it is non-smooth. For example, the curved surfaces of spherical and cylindrical shapes are smooth, while the thin wall and cuboid shapes in Fig. 3 are non-smooth since any curve crossing the edges would be non-smooth. In general, non-smooth shapes contain edges and corners, which are directly associated with sharp changes in their deviation surfaces.

The proposed mathematical decomposition procedure leads to an additive model. Due to the flexibility and interpretability of additive models, they are extensively used in diverse applications such as ecology [37], health care [38], [39], machine learning [40], and geomorphology [41]. For shape deviation at the ith location of part j, a general additive model can be defined as

$$y(\boldsymbol{x}_i, \boldsymbol{s}_j, \boldsymbol{p}_j) = \mu(\boldsymbol{x}_i, \boldsymbol{s}_j, \boldsymbol{p}_j) + \eta(\boldsymbol{x}_i, \boldsymbol{s}_j, \boldsymbol{p}_j) + \epsilon, \quad (1)$$

where y is the shape deviation, $\boldsymbol{x}$ are location covariates, $\boldsymbol{p}_j$ are the process parameters or part-independent covariates such as materials and process characteristics, $\boldsymbol{s}_j$ represents the

geometric information or part-dependent covariates, μ models the mean pattern of the shape deviation, η is a zero-mean random field that captures the spatial correlation, and ϵ is the measurement error. In the rest of this work, we drop $\boldsymbol{p}_j$ for notation simplicity since only one specific printing process is investigated in this work.

For 2D shape deviations, Huang *et al.* [13] considered the regular polygons as being carved out from their circumscribed circles through the additive model

$$\mu(\boldsymbol{x}_i, \boldsymbol{s}_j) = \mathrm{f}_1(\boldsymbol{x}_i) + \mathrm{f}_2(\boldsymbol{x}_i, \boldsymbol{s}_j) + \mathrm{f}_3(\boldsymbol{x}_i, \boldsymbol{s}_j), \tag{2}$$

where f_1 describes the shape deviation of disks, f_2 is a 2D cookie-cutter function that links the deviation profiles of circular and polygonal shapes, and f_3 is a high-order term for the remaining pattern.

To extend the model (2) to 3D cases, the mean pattern μ for 3D shape deviation follows the same decomposition formulation in Eq. (2). The main difference is that f_1 now describes the deviation profile of the smooth 3D base shape, f_2 is a 3D cookie-cutter function that connects smooth and non-smooth geometries, and f_3 is a high-order term. For example, we can use f_1 to model the shape deviation of the smooth base shape (e.g. domes), f_2 to capture the differences between the smooth base and non-smooth geometries such as thin walls (Fig. 3), and f_3 to illustrate the high-order pattern.

B. Convolution Framework as a Baseline for Smooth Shape Deviation Modeling

A convolution learning framework proposed in [9] can be used to identify the baseline function for shape deviation modeling of convex smooth shapes as

$$y(\boldsymbol{x}) = (f * g)(\boldsymbol{x}) + \eta(\boldsymbol{x}) + \epsilon, \tag{3}$$

where $\mu = f * g$, f is the input function describing the 2D shape deviation in a horizontal layer, g is the interaction function that models complex layer-to-layer interactions, η is a zero-mean GP capturing spatial correlations in the deviation profile, and ϵ is the measurement error following a zero-mean normal distribution. The variable $\boldsymbol{x}$ is the spatial location of the points in SCS, i.e., $\boldsymbol{x} = (r, \theta, \varphi)$, where θ is the polar angle and φ is the azimuth angle. The printed shape of a product is treated as the functional response $r(\theta, \varphi)$ and the nominal shape is denoted as $r_0(\theta, \varphi)$. Then shape deviation is defined as $y(\boldsymbol{x}) = r(\theta, \varphi) - r_0(\theta, \varphi)$, where $\theta \in [0, 2\pi)$, and $\varphi \in [0, \pi/2]$.

To specify μ, the first step is to identify the input function f. As the most common smooth geometries, spherical shape (as shown in Fig. 1(a)) are chosen as the base geometry, where each horizontal layer is a circular disk. Shape deviation for a disk of radius r_0 can often be modeled with a few Fourier basis functions due to its geometric simplicity, for example, $f(r_0, \theta) = c_1(r_0) + c_2(r_0)\cos(2\theta)$ in an SLA process studied by [4]. Using this formulation, Huang *et al.* [9] modeled the deviation of a dome shape as

$$\mu(r_0, \theta, \varphi) = \alpha_0(r_0) + \alpha_1(r_0)(f * g)(\theta, \varphi). \tag{4}$$

The size factors $c_1(r_0)$ and $c_2(r_0)$ can be absorbed in $\alpha_0(r_0)$ and $\alpha_1(r_0)$ in Eq. (4). Since each layer of a dome shape has radius $r_0 \sin\varphi$, the input function for the domes can be normalized, for example, as

$$f(\theta, \varphi) = \cos(2\theta)\sin\varphi. \tag{5}$$

For the layer interaction function $g(\boldsymbol{x})$, lasso regression was adopted for model selection [42]:

$$\min_{\boldsymbol{c}} \ \frac{1}{N}\sum_{i=1}^{N}\left(y_i - \sum_j c_j (f * g_j)(\theta_i, \varphi_i)\right)^2 + \gamma\,||\boldsymbol{c}||_1, \tag{6}$$

where N is the number of sampled points, $g_j(\theta, \varphi)$ is a 2D Fourier basis, and c_j is the coefficient of the basis function g_j. Significant terms shared among all domes were selected resulting in the layer interaction function

$$g(\theta, \varphi) = \cos(n_1\varphi)[1 + \cos(n_2\theta + \psi)]. \tag{7}$$

C. Association Between Smooth and Non-Smooth Geometries: 3D Cookie-Cutter Function

The convolution operator alone is inadequate to capture the sharp transitions observed in the deviation profiles around the corners of non-smooth polyhedral shapes (Fig. 2). We propose to use a 3D cookie-cutter function to subtractively carve out the deformation profile of a non-smooth shape from that of a smooth baseline shape. For example, a polygon is cut out from its minimum bounding circle for each horizontal layer as shown in Fig. 4(a). Similar to [13] and [20], the minimum bounding circle is employed as the smooth base shape since the circumcircle, which passes through all vertices of the polygon, may not exist for an arbitrary polygon.

To represent the proposed learning framework as an additive model, we define the basis functions: $h_1(\boldsymbol{x}) = (f * g)(\boldsymbol{x})$ describing smooth base shape deviation, $h_2(\boldsymbol{x})$ being the 3D cookie-cutter function linking the smooth and non-smooth geometries, and a high-order term $h_3(\boldsymbol{x})$ for the remaining pattern. Then, the learning framework can be written as

$$\mu(\boldsymbol{x}) = \alpha_0(\boldsymbol{x}) + \sum_{j=1}^{3}\alpha_j(\boldsymbol{x})h_j(\boldsymbol{x}) \tag{8}$$

where α_j, $j = 0, \ldots, 3$ represent size effects h_1 can be learned from smooth products as in [9], and both h_2 and h_3 are fully determined by the geometries of AM-fabricated products. Note that because we use convex smooth shapes as the bases, we can infer the shape deviation of convex polyhedra while the shape distortion of concave geometries (e.g., pentagram in 2D) needs to be studied using a concave smooth geometry as the baseline.

For the 2D case, [13] applied two candidate 2D cookie-cutter functions h_2 as the association function to carve out regular polygons from their circumcircles: the square-wave function

$$sq(\theta) = \mathrm{sign}\{\cos[n(\theta - \phi_0)/2]\}, \tag{9}$$

and the sawtooth-wave function

$$sw(\theta) = (\theta - \phi_0)\mathrm{MOD}(2\pi/n), \tag{10}$$

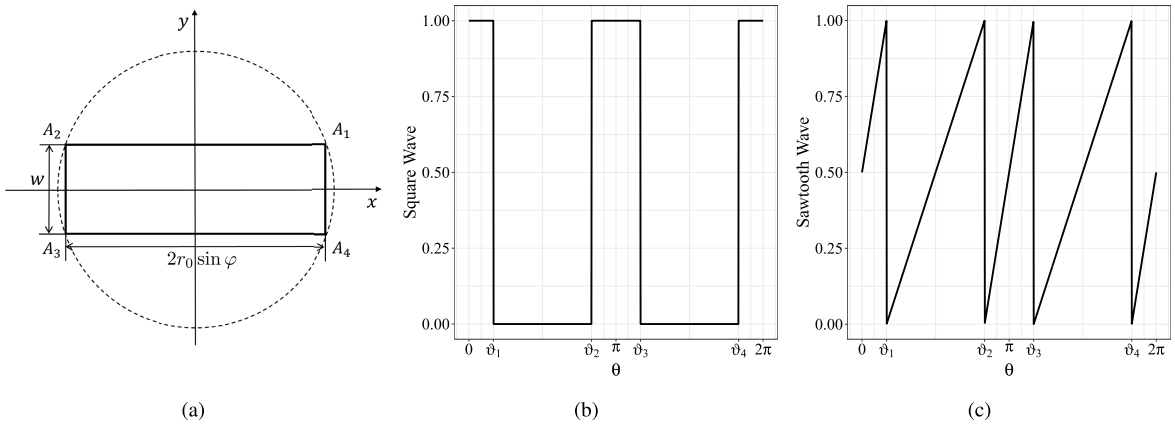

Fig. 4. (a) A rectangle cut from its circumcircle and corresponding (b) 2D square-wave cookie-cutter function and (c) 2D sawtooth-wave cookie-cutter function.

where n is the number of sides and ϕ_0 is a phase term to shift the cutting position. These functions allow sharp transitions on the deformation patterns near the corners.

A generalization of the sawtooth-wave function was established in [14] as

$$sw(\theta) = \frac{\pi(\theta - \vartheta_{j-1})\text{MOD}(\vartheta_j - \vartheta_{j-1})}{2(\vartheta_j - \vartheta_{j-1})} \tag{11}$$

for selected angles ϑ_j, $j = 1, \ldots, n$. Note that such function is only needed when the interior angle of a corner is less than $\pi/6$ according to their experimental studies.

For the 3D case with more complex geometries, we apply the 2D cookie-cutter function in each horizontal layer defined by φ in SCS by modifying the frequency of the square-wave or sawtooth-wave function such that the amplitudes alternate at the sharp corners defined by $\vartheta_j(\varphi)$, $j = 1, \ldots, n$. Thus, one candidate for h_2 is the 3D square-wave function

$$sq(\theta, \varphi) = \frac{1}{2}\left\{\text{sign}\left[\sin\left(\frac{(-1)^{j+1}\pi\theta}{\vartheta_j(\varphi)}\right)\right] + 1\right\}, \tag{12}$$

and the other alternative is 3D sawtooth-wave function

$$sw(\theta, \varphi) = \frac{\theta - \vartheta_{j-1}(\varphi)}{\vartheta_j(\varphi) - \vartheta_{j-1}(\varphi)}, \tag{13}$$

for $\vartheta_{j-1}(\varphi) \le \theta < \vartheta_j(\varphi)$, $j = 1, \ldots, n+1$, where $\vartheta_j(\varphi)$, $j = 1, \ldots, n$ are the polar angles of sharp transitions with $\vartheta_0(\varphi) = 0$ and $\vartheta_{n+1}(\varphi) = 2\pi$.

The proposed 3D cookie-cutter functions can be regarded as the stack of 2D cookie-cutter functions over the φ-direction, where each layer could have sharp transitions at different angles according to the designed geometry. As the number of corners increases and the polyhedron approaches a sphere, the sharp corners effectively vanish and h_2 is approximately constant in both definitions.

In the motivating example, a thin wall with a half-cylindrical shape has radius r_0 and thickness w (Fig. 5), where each horizontal layer is a rectangle with length $2r_0 \sin\varphi$ and width w. To cut out a rectangle defined by the corner points (A_1, A_2, A_3, A_4) from its circumcircle as shown in Fig. 4(a), we first find the angles of each corner as $\vartheta_1, \vartheta_2, \vartheta_3$ and ϑ_4, then the corresponding 2D square-wave function is shown in Fig. 4(b) and 2D sawtooth-wave function is shown in Fig. 4(c).

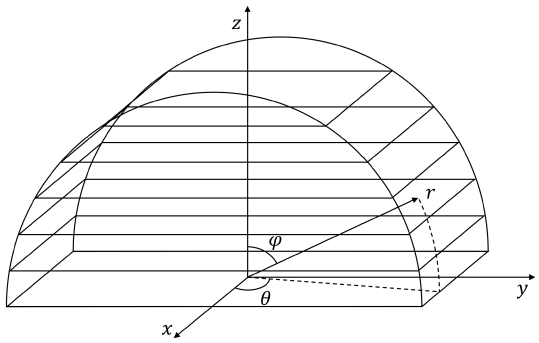

Fig. 5. A thin wall fabricated by stacking rectangles.

Since the rectangle sizes in each horizontal layer defined by φ are different, the sharp transitions for each layer happen at different polar angles, which are purely defined by the geometry of the product. The scatter plots of proposed 3D square-wave and sawtooth-wave cookie-cutter functions are shown in Fig. 6.

While the same thin-wall parts are treated as 2D shapes in [9], they are regarded as 3D shapes in this work. Unlike the deviation profiles $y(\varphi)$ for 2D cases, shape deviations of 3D non-smooth thin walls show deviation surfaces $y(\theta, \varphi)$ in SCS (Fig. 2). Furthermore, to predict the shape deviation of these thin walls on the front, back, and curved top surfaces, each thin wall is regarded as the stack of rectangles of different sizes (Fig. 5), which requires the 3D cookie-cutter function in Eq. (12) and Eq. (13).

D. Spatial Correlation Modeling With a Novel Distance Metric for Heterogeneous Shape Data

The random field η in model (1) is intended to capture the spatial correlations among deformed regions. It is frequently assumed to be a zero-mean GP with a squared-exponential kernel [43]

$$k(\boldsymbol{x}_i, \boldsymbol{x}_j) = \exp\left(-\frac{d(\boldsymbol{x}_i, \boldsymbol{x}_j)^2}{\delta}\right), \tag{14}$$

where $d(\boldsymbol{x}_i, \boldsymbol{x}_j)$ is the distance between $\boldsymbol{x}_i$ and $\boldsymbol{x}_j$.

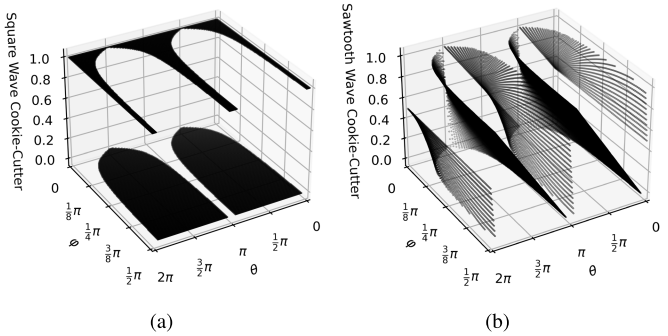

Fig. 6. (a) 3D square-wave function and (b) 3D sawtooth-wave function for the 0.8-inch thin wall.

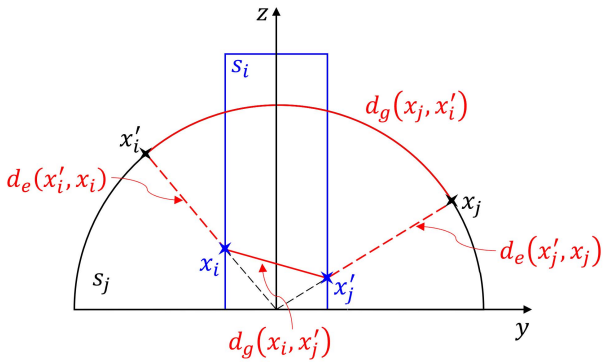

Fig. 7. Proposed distance metric between $\boldsymbol{x}_i$ on shape s_i (in blue) and $\boldsymbol{x}_j$ on shape s_j (in black).

The challenge, however, is to learn the spatial correlation not only among regions of the same product but also across heterogeneous shapes.

For convenience, the spatial correlation between two sample points in the $\mathbb{R}^3$ space is described in the Cartesian coordinate system, i.e., $\boldsymbol{x}_i = (x_i, y_i, z_i)$ rather than the SCS. Note that it is feasible to establish the GP in the SCS as well. The coordinates are scaled to the current coordinate over the maximum in each direction. Note that $(0, 0, 0)$ corresponds to the center of the printing bed, and the maximum height was chosen to eliminate the effect of different scales in the z direction.

Due to the physics involved in generating and measuring the shape deviation, Sun *et al.* [44] and Castillo *et al.* [45] pointed out that geodesic distance, which is defined as the shortest distance between points on a 3D surface, is a better measure of the spatial correlation in the same additively manufactured part rather than the Euclidean distance. A thorough review of geodesic paths and distances on the surface of triangle meshes can be found in [46]. Due to the high computational cost of the geodesic distance, we employ the as-rigid-as-possible parameterization to first map the surface into a 2D plane, and then the point-to-point geodesic distance can be approximated by the corresponding Euclidean distance [47]. However, one challenge is that there is no clear definition of geodesic distance among different parts since such path along the surface does not exist.

For two points $\boldsymbol{x}_i$ and $\boldsymbol{x}_j$ lying on the surfaces of two shapes s_i and s_j, respectively, we propose a new distance metric

$$d(\boldsymbol{x}_i, \boldsymbol{x}_j) = \frac{1}{2}\Big[d_e(\boldsymbol{x}_i, \boldsymbol{x}_i') + d_g(\boldsymbol{x}_i', \boldsymbol{x}_j) + d_e(\boldsymbol{x}_j, \boldsymbol{x}_j') + d_g(\boldsymbol{x}_j', \boldsymbol{x}_i)\Big] \quad (15)$$

where $\boldsymbol{x}_i'$ is the projection of point $\boldsymbol{x}_i$ onto shape s_j, i.e., $\boldsymbol{x}_i'$ and $\boldsymbol{x}_i$ have the same angles (θ_i, φ_i), then $\boldsymbol{x}_j$ and $\boldsymbol{x}_i'$ are points on the same part with a properly defined geodesic distance $d_g(\boldsymbol{x}_i', \boldsymbol{x}_j)$. Similarly, $\boldsymbol{x}_j'$ and $\boldsymbol{x}_j$ are on the line defined by the angles (θ_j, φ_j) and d_e is the standard Euclidean distance.

For example, considering the side view of a thin wall and a dome shape as shown in Fig. 7, the proposed distance is the combination of four red paths, where the solid curves denoting the geodesic distances d_g and the dashed ones are the Euclidean distances d_e. By adding the projection distance $d_e(\boldsymbol{x}_j', \boldsymbol{x}_j)$ and $d_e(\boldsymbol{x}_i', \boldsymbol{x}_i)$, we complete a circuit from $\boldsymbol{x}_i$ to $\boldsymbol{x}_j$ and back which ensures that d is a valid distance measure. Another advantage of Eq. (15) is that, if two shapes s_i and s_j are the same, the projection distances are zero, and then the proposed distance is the standard geodesic distance.

III. Sequential Model Estimation Procedure for the Unified Modeling Framework

After specifying each component of the additive model, a sequential model fitting strategy is proposed to efficiently estimate the model parameters, mitigate over-fitting, and transfer the knowledge from smooth base shape to non-smooth polyhedral shapes.

In general, the parameter estimation procedure follows a similar strategy to the boosted models [48] of fitting models sequentially based on the residuals of earlier models. As specified in [9], the convolution h_1 describes the shrinkage of smooth geometries during printing caused by material phase changes, inter-layer interactions, and gravity effects. On the other hand, the deviation profiles of non-smooth shapes exhibit sharp transitions introduced by uneven thermal stresses around the corners [35]. By regarding the non-smooth shape as being cut from a set of smooth patches, we apply the 3D cookie-cutter function h_2 to capture the sharp transitions and h_3 to model the difference in deviation profiles between smooth and non-smooth geometries. Thus, the smooth shape deviation is modeled first to build the baseline model, while non-smooth parts are included later to assess the association and remaining pattern.

In the final step, we use GP regression (GPR) to model η for the following reasons: (1) estimating GP parameters is computationally expensive; (2) the full training set is involved since spatial correlation affects all shapes; and (3) due to the flexibility of GP, the main effect μ could be confounded, which compromises the insights from the parametric model.

To be more specific, after dividing the data $\mathcal{D} = (y, \boldsymbol{x})$ into $\mathcal{D}^0$ for smooth shapes and $\mathcal{D}^1$ for non-smooth shapes, there are three steps to fit the model sequentially. First, we estimate the parameters in α_0, α_1 and h_1 of Eq. (8) using the data in $\mathcal{D}^0$. Since only smooth shapes are involved, the model is reduced to $y = \alpha_0 + \alpha_1 h_1 + \epsilon$. Second, non-smooth shape deviations in $\mathcal{D}^1$ are used to estimate the parameters in α_2 and α_3 with

Algorithm 1 Process-Informed Sequential Model Fitting Strategy

Split data $\mathcal{D}$ into $\mathcal{D}^0$ (smooth) and $\mathcal{D}^1$ (non-smooth) according to design geometry;
Initialize the parameters γ for h_1;
Fit the parameters for the model $y(\boldsymbol{x}) = \alpha_0(\boldsymbol{x}) + \alpha_1(\boldsymbol{x})h_1(\boldsymbol{x}) + \epsilon, \forall(y, \boldsymbol{x}) \in \mathcal{D}^0$;
Calculate residuals $\tilde{y} = y(\boldsymbol{x}) - \big(\hat{\alpha}_0(\boldsymbol{x}) + \hat{\alpha}_1(\boldsymbol{x})\hat{h}_1(\boldsymbol{x})\big), \forall(y, \boldsymbol{x}) \in \mathcal{D}$;
Fit the parameters for the model $\tilde{y} = \alpha_2(\boldsymbol{x})h_2(\boldsymbol{x}) + \alpha_3(\boldsymbol{x})h_3(\boldsymbol{x}) + \epsilon, \forall(y, \boldsymbol{x}) \in \mathcal{D}^1$;
Calculate residuals $\tilde{\tilde{y}} = \tilde{y} - (\hat{\alpha}_2(\boldsymbol{x})h_2(\boldsymbol{x}) + \hat{\alpha}_3(\boldsymbol{x})h_3(\boldsymbol{x})), \forall(y, \boldsymbol{x}) \in \mathcal{D}$;
Calculate pairwise distance $d(\boldsymbol{x}_i, \boldsymbol{x}_j), \forall \boldsymbol{x}_i, \boldsymbol{x}_j \in \mathcal{D}$
Fit a GP for model $\tilde{\tilde{y}} \sim \mathcal{N}\big(0, k(d(\boldsymbol{x}_i, \boldsymbol{x}_j))\big)$

respect to the residuals $\tilde{y} = y - (\hat{\alpha}_0 + \hat{\alpha}_1\hat{h}_1)$. Recall that h_2 and h_3 are determined by the geometry, and the model is $\tilde{y} = \alpha_2 h_2 + \alpha_3 h_3 + \epsilon$ for the non-smooth shape deviations. Lastly, to model the spatial correlation, GPR techniques are applied to model the residuals $\tilde{\tilde{y}} = \tilde{y} - (\hat{\alpha}_2 h_2 + \hat{\alpha}_3 h_3)$ from all data with $h_2 = 0$ and $h_3 = 0$ for smooth parts, i.e., $\tilde{\tilde{y}} \sim \mathcal{N}(0, k(\cdot, \cdot))$. By learning these three components sequentially, we can predict the shape deviation of untried products. The proposed parameter estimation strategy is summarized in Algorithm 1.

Furthermore, if $\alpha_k, k = 0, \ldots, 3$, have a parametric form, the model parameters can be estimated using the profile likelihood approach. Without loss of generality, assume that $\alpha_k(\boldsymbol{x})$ is a basis expansion of the form $\alpha_k(\boldsymbol{x}) = \sum_{j=1}^{J_k} q_k^j(\boldsymbol{x})\beta_k^j$. Then, the model can be expressed as

$$\boldsymbol{y} = \mathbf{H}(\gamma)\boldsymbol{\beta} + \boldsymbol{\eta} + \boldsymbol{\epsilon}, \tag{16}$$

where

$$\mathbf{H}(\boldsymbol{\gamma}) = \Big(q_0^1(\boldsymbol{x}), \ldots, q_0^{J_0}(\boldsymbol{x}), q_1^1(\boldsymbol{x})\boldsymbol{h_1}(\boldsymbol{\gamma}), \ldots, q_3^{J_3}(\boldsymbol{x})\boldsymbol{h_3}\Big)$$

and

$$\boldsymbol{\beta} = \big(\beta_0^1, \ldots, \beta_0^{J_0}, \beta_1^1, \ldots, \beta_3^{J_3}\big)^{\intercal}.$$

The maximum likelihood estimates (MLE) are obtained by solving

$$\begin{aligned} &\min_{\boldsymbol{\gamma}} \ \frac{1}{2\sigma^2}||\boldsymbol{y} - \mathbf{H}_1(\gamma)\hat{\boldsymbol{\beta}}'||^2 + \frac{n}{2}\ln(\sigma^2) \\ &\text{s.t. } \hat{\boldsymbol{\beta}}' = \big(\mathbf{H}_1^{\intercal}(\boldsymbol{\gamma})\mathbf{H}_1(\boldsymbol{\gamma})\big)^{-1}\mathbf{H}_1^{\intercal}(\boldsymbol{\gamma})\boldsymbol{y} \end{aligned} \tag{17}$$

where $\boldsymbol{y}$ is the shape deviation of observations included in $\mathcal{D}^0$, n is the total number of points in $\mathcal{D}^0$, $\mathbf{H}_1$ is the matrix of the first $J_0 + J_1$ columns of $\mathbf{H}$, and $\boldsymbol{\beta}' = (\boldsymbol{\beta}_0, \boldsymbol{\beta}_1)$. For the parameters of α_2 and α_3, the MLE is

$$\hat{\boldsymbol{\beta}}'' = \big(\mathbf{H}_2^{\intercal}\mathbf{H}_2\big)^{-1}\mathbf{H}_2^{\intercal}(\boldsymbol{\gamma})\tilde{\boldsymbol{y}}$$

where $\tilde{\boldsymbol{y}}$ is as defined in Algorithm 1 for observations in $\mathcal{D}^1$, $\mathbf{H}_2$ is the matrix of the last $J_2 + J_3$ columns of $\mathbf{H}$, and $\boldsymbol{\beta}'' = (\boldsymbol{\beta}_2, \boldsymbol{\beta}_3)$.

IV. Case Study: Shape Deviation Modeling and Estimation for Domes and Thin Walls

In this section, we revisit the motivating example in Sec. I to demonstrate the capability of the proposed learning framework for modeling and predicting the shape deviation patterns of a wide variety of geometries containing both smooth and non-smooth features in AM. Seven parts (Fig. 1) were printed through the mask image projection stereolithography (MIP-SLA) process. After the printing process, a ROMER absolute arm with RS4 laser scanner is used to collect the measurements as point clouds, which are then registered using the constrained iterative closest point algorithm [49]. The printing quality is evaluated by the shape deviation surface of each part [9] as illustrated in Fig. 2. We employ all domes and 0.8-inch and 2.0-inch thin walls as the training set and leave the 1.5-inch thin wall as the validation set.

To implement the learning framework in Eq. (8), the first step is to identify the input function f. Note that, due to machine repair, the pattern of shape deviation of 2D circular disks changed from what was presented in [4], i.e., the input function $f(\theta, \varphi)$ should have a different pattern and we need to fit the spherical shape model for the new data. Luan and Huang [14] defined the new pattern as

$$f(\theta) = \cos\Big(2\theta + \frac{\pi}{3}\Big)\mathbf{1}_{\theta\in[0,\pi)} - \sin(2\theta)\mathbf{1}_{\theta\in[\pi,2\pi)}. \tag{18}$$

Recall that the form of input function was changed to Eq. (5) by multiplying it by $\sin\varphi$ because the radius of each layer is $r_0 \sin\varphi$ for the dome shape. Similarly, we have the input function $f(\theta, \varphi)$ for spherical shapes as

$$f(\theta, \varphi) = f(\theta)\sin\varphi. \tag{19}$$

If the radius is r_0 and the thickness is w for the thin wall shape, the circumcircle radius for each horizontal layer φ is

$$\max_{\theta}\{r_0(\theta, \varphi)\} = \sqrt{r_0^2\sin^2\varphi + \Big(\frac{w}{2}\Big)^2} \approx r_0\sin\varphi, \tag{20}$$

since w is much smaller than r_0 for the thin products. Then, we can compute the convolution explicitly and regard the thin walls as cut from the domes with the same radii, and the same input function $f(\theta, \varphi)$ as in Eq. (19) can be applied. For the layer interaction function $g(\theta, \varphi)$, Eq. (7) is used since the printing mechanism is the same and only the shapes and sizes change. Thus, h_1 is fully specified.

Next, we need to specify the sharp transition angles ϑ_j and n used in the 3D cookie-cutter function h_2 in Eq. (12). As shown in Fig. 4, $n = 4$ and the angles are $\vartheta_1 = \arctan(w/(2r_0\sin\varphi))$, $\vartheta_2 = \pi - \vartheta_1$, $\vartheta_3 = \pi + \vartheta_1$, $\vartheta_4 = 2\pi - \vartheta_1$ according to the geometry of the thin walls.

To capture the arch pattern of thin walls presented in the deviation profiles in Fig. 2, we choose h_3 as

$$\begin{aligned} h_3(\theta, \varphi) = \Big\{&\sin\Big(\frac{n}{4}\theta\Big)\mathbf{1}_{\theta\in[\vartheta_1,\vartheta_2)} \\ &+ \sin\Big[\frac{n}{4}(\theta - \pi)\Big]\mathbf{1}_{\theta\in[\vartheta_3,\vartheta_4)}\Big\}\sin\varphi, \end{aligned} \tag{21}$$

where n is the number of sides. For the thin walls, we have $n = 4$, and when $n \to \infty$, this term becomes white noise.

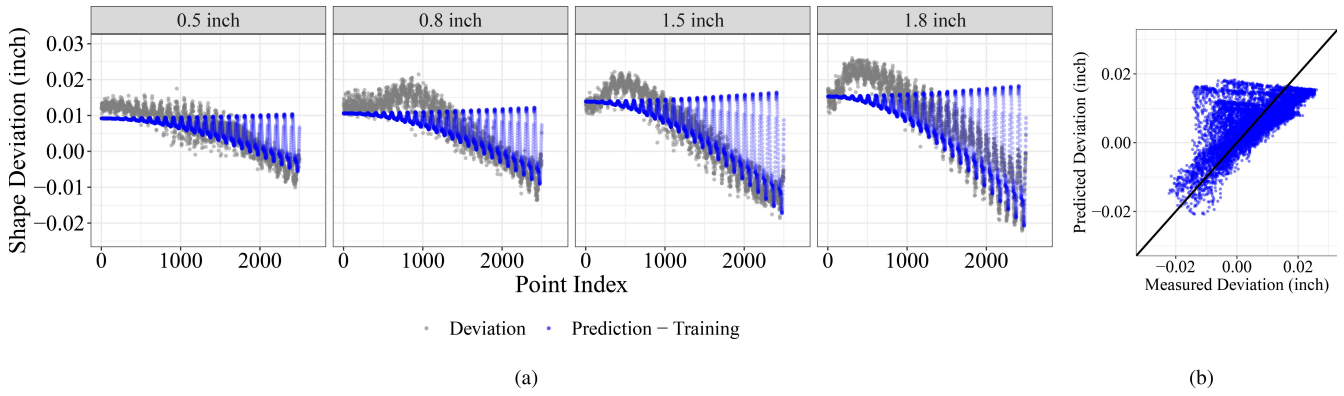

Fig. 8. Measured shape deviation (in gray) and model prediction (in blue) for domes.

Due to the limited number of samples, we follow similar linear assumptions as in [9] to incorporate the size effect. Denoting $\boldsymbol{x} = (x, y, z, r_0, \theta, \varphi)$, which contains the location information of Cartesian coordinates and spherical coordinates, the conjectures are

1) $n_1(\boldsymbol{x}) = c_1 + c_2 r_0$,
2) n_2 and ψ are unknown constants,
3) $\alpha_0(\boldsymbol{x}) = \beta_{0,1} + \beta_{0,2} r_0$,
4) $\alpha_1(\boldsymbol{x}) = \beta_{1,1} + \beta_{1,2} r_0$,
5) $\alpha_2(\boldsymbol{x}) = \beta_{2,1} + \beta_{2,2}\left[\sqrt{r_0^2 \sin^2\varphi + w^2/4} - r_0(\theta, \varphi)\right]$
6) $\alpha_3(\boldsymbol{x}) = \beta_{3,1} + \beta_{3,2} r_0$.

Note that n_1, n_2, and ψ are the parameters in the layer interaction function g as in Eq. (7), while $\alpha_i, i = 0, \ldots, 3$, are the coefficients describing the size effect in Eq. (8). The first four conjectures are for the baseline model, and the last two would affect the 3D cookie-cutter function. For simplicity, we assume the layer-to-layer interactions change for different sizes mainly along the φ-direction and are related to the number of layers printed, thus n_1 deciding the period over φ is assumed to be proportional to the size, while n_2 and ψ control the period and phase in θ-direction is assumed to be constant.

To achieve better model interpretability, a linear relationship to the size of the product is imposed on the coefficients of α_0, α_1 and α_3. As the coefficient of cookie-cutter term, α_2 is proportional to the cutting width, i.e., the difference between the circumcircle radius and polygonal shape at each angle, which is $\sqrt{r_0^2 \sin^2\varphi + w^2/4} - r_0(\theta, \varphi)$. Under these assumptions, at least two samples of each shape are required to estimate the model parameters. Because a limited number of training samples are usually provided in AM, more complex relationships for α require knowledge of the material and process interactions.

The MLE procedure described in Sec. III is employed to fit the spherical shape deviation model through the *mle2* function in the R package *bbmle* with randomized initialization in the parameter space, and the results are given in Table I and Fig. 8. The mean absolute error (MAE) is 0.0048 and the root mean square error (RMSE) is 0.0065. We plot the shape deviation by point index due to the difficulty of comparing model fitting performance in 3D space. The four blocks from the left correspond to the 0.5-inch, 0.8-inch, 1.5-inch, and 1.8-inch domes, respectively. The predictions are close to the actual deviation measurements, except at the upper right corner. Note that the results are different from [9] since the input function $f(\theta, \varphi)$ is changed to Eq. (19). The estimates of c_1 and c_2 are not statistically different from zero and the layer interaction function can be simplified as $g(\theta, \varphi) = 1 + \cos(n_2\theta + \psi)$.

TABLE I
PARAMETER ESTIMATES AND STANDARD ERROR (SE) FOR THE DEVIATION OF DOME SHAPES

Parameters	Estimate	SE
n_2	0.6462	0.006591
ψ	4.0793	0.019610
c_1	0.0034	0.230790
c_2	-0.0016	0.169782
$\beta_{0,1}$	0.0068	0.000210
$\beta_{0,2}$	0.0047	0.000166
$\beta_{1,1}$	0.0063	0.000601
$\beta_{1,2}$	0.0158	0.000476
σ	0.0065	0.000046

Next, the thin walls with radii of 0.8 inch and 2.0 inches are used as the training set, and the 1.5-inch thin wall is left as the validation set. The estimated model parameters for α_2 and α_3 are shown in Table II, and the measured deviations versus model predictions are presented in Fig. 9 for both square-wave and sawtooth-wave cookie-cutter functions. The model performance metrics are summarized in Table III. From both figures and performance metrics, the square wave function is better than the sawtooth-wave function for modeling the shape deviation of thin walls. Thus, we use the square-wave function for the remainder of the paper. Since both $\beta_{2,2}$ and $\beta_{3,2}$ are positive, we can infer that the effects of the sharp transition and arch pattern on the deviation profile increase with the part's size. However, there are some remaining spatial patterns to be captured, so the residuals are fitted through GPR with squared-exponential kernel in Eq. (14) using Euclidean distance between points through the *gam* function in the R package *mgcv*.

The measurements and model predictions are presented in Fig. 10 and Table IV. For the dome parts, not only the upper

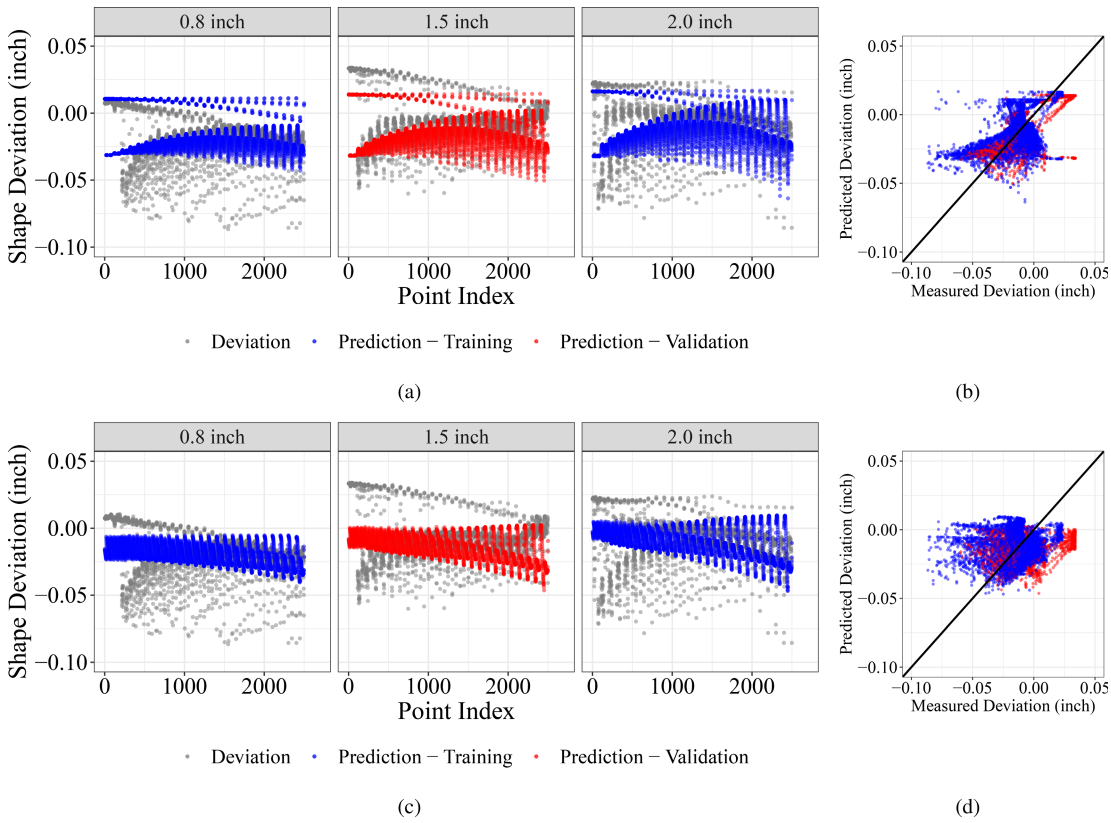

Fig. 9. Measured shape deviation (in gray), training set prediction (in blue) and validation set prediction (in red) for thin walls applying (a and b) square wave and (c and d) sawtooth wave functions.

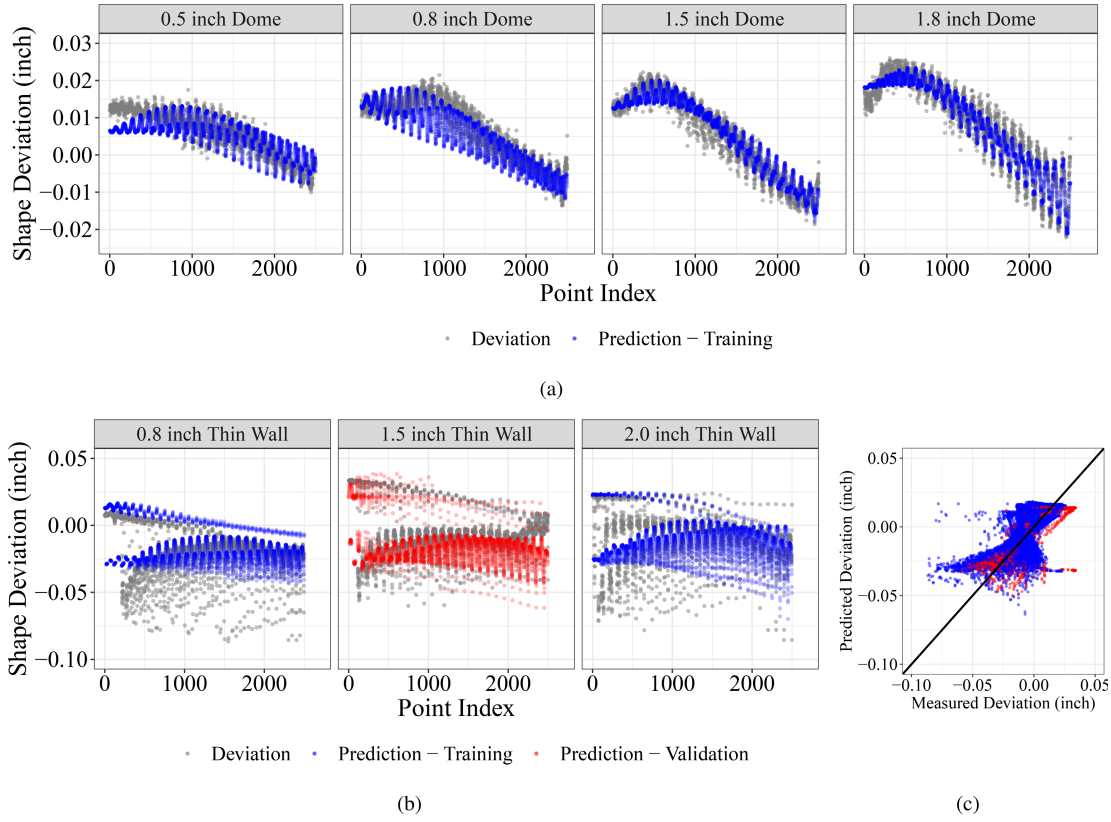

Fig. 10. Measured shape deviation (in gray), training set prediction (in blue) and validation set prediction (in red) after GPR with Euclidean distance.

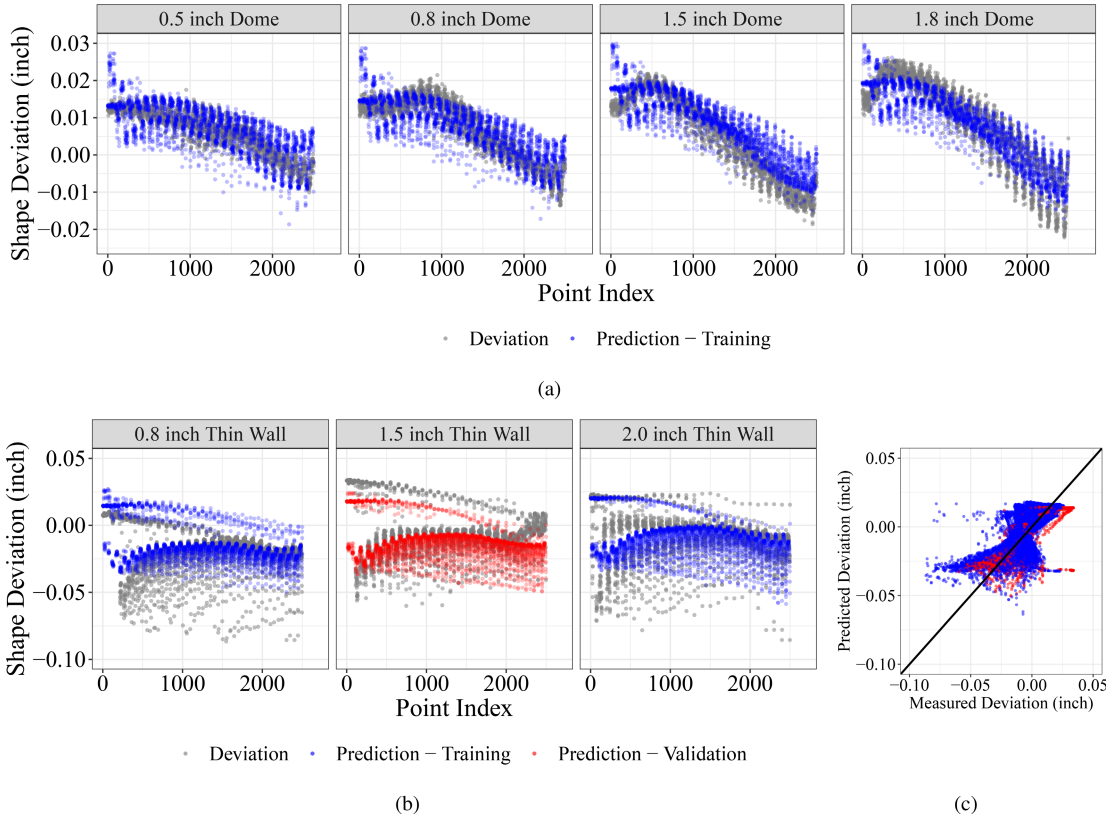

Fig. 11. Measured shape deviation (in gray), training set prediction (in blue) and validation set prediction (in red) after GPR with the proposed distance.

TABLE II
PARAMETER ESTIMATES AND STANDARD ERROR (SE) FOR COOKIE-CUTTER AND HIGH-ORDER TERMS

Parameters	Square Wave		Sawtooth Wave	
	Estimate	SE	Estimate	SE
$\beta_{2,1}$	-0.0387	0.00106	-0.0041	0.00123
$\beta_{2,2}$	0.0002	0.00004	-0.0003	0.00004
$\beta_{3,1}$	0.0124	0.00175	-0.0040	0.00184
$\beta_{3,2}$	0.0139	0.00074	0.0137	0.00093

TABLE III
THIN WALL MODEL PERFORMANCE APPLYING DIFFERENT COOKIE-CUTTER FUNCTIONS

Cookie-Cutter	Training		Validation	
	MAE	RMSE	MAE	RMSE
Square Wave	0.0122	0.0160	0.0120	0.0158
Sawtooth Wave	0.0156	0.0200	0.0164	0.0205

right corners in Fig. 8 have been offset by GP, the expansion of the larger domes are correctly predicted. Predictions for thin walls are improved from the results in Fig. 9, and the performance metrics (MAE and RMSE) are reduced for both training and validation sets.

Since the GP combines the location information of all shapes together, and points on the smaller domes are closer

TABLE IV
MODEL PERFORMANCE COMPARISON

Model	Training		Validation	
	MAE	RMSE	MAE	RMSE
Parametric	0.0122	0.0160	0.0120	0.0158
Parametric + Euclidean Distance	0.0050	0.0093	0.0107	0.0148
Parametric + Proposed Distance	0.0060	0.0095	0.0087	0.0124

to those on the thin walls, their deviation predictions are greatly affected by the deviation pattern of thin walls. Thus, the 0.5-inch and 0.8-inch domes show a wider variation of the deviation prediction compared with the 1.5-inch and 1.8-inch domes. This suggests that the spatial correlation among different shapes is overestimated, and we can improve the spatial correlation modeling by modifying the distance metric in the squared-exponential kernel as specified in Sec. II-D.

After computing the proposed geodesic distance among all shapes and estimating the spatial correlation with the *mKrig* function in the R package *fields*, the updated model prediction and performance are shown in Fig. 11 and Table IV. With the proposed distance metric considering both geographic and geometric information, the GP accurately captures the spatial correlation. Though the deviations of the first few points in domes are overestimated, predictions cover most of the actual deviation measurements in the training set. With slightly worse training set performance, the performance on the validation

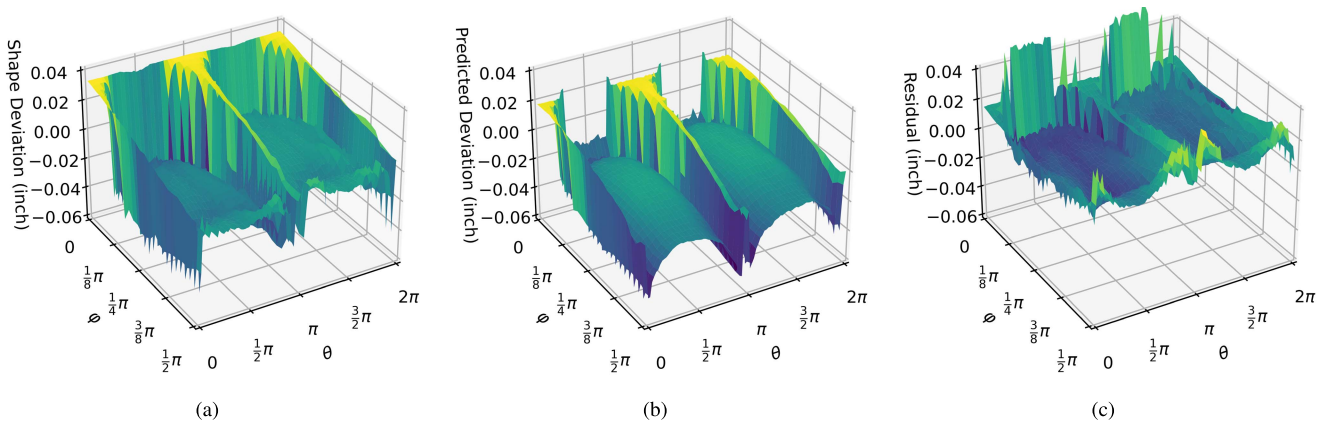

(a) (b) (c)

Fig. 12. (a) Measured shape deviation, (b) predicted shape deviation, and (c) residuals for the 1.5-inch thin wall (darker/lighter color for negative/positive deviation).

set improved around 20% using the proposed distance metric. The measured shape deviation, predicted deviation surface, and residuals of the final model with GPR using the proposed distance metric are presented in Fig. 12.

V. Conclusion

This work establishes a unified learning framework for shape deviation modeling and learning of smooth and non-smooth 3D geometries in AM. It is accomplished by mathematically decomposing the AM process into an additive step to build a smooth base shape, and a subtractive step to carve out non-smooth shapes from the base shape. The unified shape accuracy model contains the baseline deviation of smooth base shapes, sharp transitions caused by the subtractive step, spatial correlation, and residual term. The previously proposed convolution framework serves as the baseline model for smooth shapes. The proposed 3D cookie-cutter function effectively captures the unique shape deviation pattern of sharp corners of non-smooth convex shapes and enables joint learning of heterogeneous deviation patterns on smooth and non-smooth geometries. A novel distance measure is proposed to model the spatial correlation among heterogeneous shapes by combining the local geodesic distance between points in the same 3D object and the Euclidean distance between projected points across 3D objects.

A case study shows that the unified model can successfully predict the shape deviation of convex smooth (domes) and non-smooth (thin walls) shapes. Since 3D freeform shapes can be approximated as a combination of smooth patches and sharp corners, the proposed learning framework builds a foundation to further extend this modeling approach to predict the quality of 3D freeform shapes. Furthermore, the strategy of connecting engineering surface data through decomposition of data generation processes can be adopted in other domains for engineering-informed learning of heterogeneous data.

Acknowledgment

The SLA experimentation was conducted at the Prof. Y. Chen's Laboratory, University of Southern California.

References

[1] T. Campbell, C. Williams, O. Ivanova, and B. Garrett, "Could 3D printing change the world? technologies, potential, and implications of additive manufacturing," Atlantic Council, Washington, DC, USA, Tech. Rep., 2011. [Online]. Available: https://www.atlanticcouncil.org/wp-content/uploads/2011/10/101711_ACUS_3DPrinting.PDF

[2] W. Gao *et al.*, "The status, challenges, and future of additive manufacturing in engineering," *Comput.-Aided Des.*, vol. 69, pp. 65–89, Dec. 2015.

[3] E. MacDonald and R. Wicker, "Multiprocess 3D printing for increasing component functionality," *Science*, vol. 353, no. 6307, Sep. 2016, Art. no. aaf2093.

[4] Q. Huang, J. Zhang, A. Sabbaghi, and T. Dasgupta, "Optimal offline compensation of shape shrinkage for three-dimensional printing processes," *IIE Trans.*, vol. 47, no. 5, pp. 431–441, 2015.

[5] A. Sabbaghi, T. Dasgupta, Q. Huang, and J. Zhang, "Inference for deformation and interference in 3D printing," *Ann. Appl. Statist.*, vol. 8, no. 3, pp. 1395–1415, Sep. 2014.

[6] Y. Jin, S. Joe Qin, and Q. Huang, "Offline predictive control of out-of-plane shape deformation for additive manufacturing," *J. Manuf. Sci. Eng.*, vol. 138, no. 12, p. 1, Dec. 2016.

[7] J. L. Bartlett, B. P. Croom, J. Burdick, D. Henkel, and X. Li, "Revealing mechanisms of residual stress development in additive manufacturing via digital image correlation," *Additive Manuf.*, vol. 22, pp. 1–12, Aug. 2018.

[8] B. Colosimo, Q. Huang, T. Dasgupta, and F. Tsung, "Opportunities and challenges of quality engineering for additive manufacturing," *J. Quality Technol.*, vol. 50, no. 3, pp. 233–252, 2018.

[9] Q. Huang, Y. Wang, M. Lyu, and W. Lin, "Shape deviation generator—A convolution framework for learning and predicting 3-D printing shape accuracy," *IEEE Trans. Autom. Sci. Eng.*, vol. 17, no. 3, pp. 1486–1500, Jul. 2020.

[10] L. N. Baldwin, K. Wachowicz, S. D. Thomas, R. Rivest, and B. G. Fallone, "Characterization, prediction, and correction of geometric distortion in 3T MR images," *Med. Phys.*, vol. 34, no. 2, pp. 388–399, Jan. 2007.

[11] Q. Huang, "An analytical foundation for optimal compensation of three-dimensional shape deformation in additive manufacturing," *J. Manuf. Sci. Eng.*, vol. 138, no. 6, pp. 1–8, Jun. 2016.

[12] M. Khanzadeh, P. Rao, R. Jafari-Marandi, B. K. Smith, M. A. Tschopp, and L. Bian, "Quantifying geometric accuracy with unsupervised machine learning: Using self-organizing map on fused filament fabrication additive manufacturing parts," *J. Manuf. Sci. Eng.*, vol. 140, no. 3, Mar. 2018, Art. no. 031011.

[13] Q. Huang, H. Nouri, K. Xu, Y. Chen, S. Sosina, and T. Dasgupta, "Statistical predictive modeling and compensation of geometric deviations of three-dimensional printed products," *J. Manuf. Sci. Eng.*, vol. 136, no. 6, pp. 1–10, Dec. 2014.

[14] H. Luan and Q. Huang, "Prescriptive modeling and compensation of in-plane shape deformation for 3-D printed freeform products," *IEEE Trans. Autom. Sci. Eng.*, vol. 14, no. 1, pp. 73–82, Jan. 2017.

[15] L. Cheng, A. Wang, and F. Tsung, "A prediction and compensation scheme for in-plane shape deviation of additive manufacturing with information on process parameters," *IISE Trans.*, vol. 50, no. 5, pp. 394–406, 2018.

[16] Y. Jin, S. J. Qin, and Q. Huang, "Modeling inter-layer interactions for out-of-plane shape deviation reduction in additive manufacturing," *IISE Trans.*, vol. 52, no. 7, pp. 721–731, Jul. 2020.
[17] N. Decker, M. Lyu, Y. Wang, and Q. Huang, "Geometric accuracy prediction and improvement for additive manufacturing using triangular mesh shape data," *J. Manuf. Sci. Eng.*, vol. 143, no. 6, pp. 1–12, Jun. 2021.
[18] A. Sabbaghi and Q. Huang, "Model transfer across additive manufacturing processes via mean effect equivalence of lurking variables," *Ann. Appl. Statist.*, vol. 12, no. 4, pp. 2409–2429, 2018.
[19] J. Francis, A. Sabbaghi, M. R. Shankar, M. Ghasri-Khouzani, and L. Bian, "Efficient distortion prediction of additively manufactured parts using Bayesian model transfer between material systems," *J. Manuf. Sci. Eng.*, vol. 142, no. 5, pp. 1–16, May 2020.
[20] A. Sabbaghi, Q. Huang, and T. Dasgupta, "Bayesian model building from small samples of disparate data for capturing in-plane deviation in additive manufacturing," *Technometrics*, vol. 60, no. 4, pp. 532–544, 2018.
[21] R. de Souza Borges Ferreira, A. Sabbaghi, and Q. Huang, "Automated geometric shape deviation modeling for additive manufacturing systems via Bayesian neural networks," *IEEE Trans. Autom. Sci. Eng.*, vol. 17, no. 2, pp. 584–598, Apr. 2020.
[22] P. K. Rao, J. Liu, D. Roberson, Z. Kong, and C. Williams, "Online real-time quality monitoring in additive manufacturing processes using heterogeneous sensors," *J. Manuf. Sci. Eng.*, vol. 137, no. 6, Dec. 2015, Art. no. 061007.
[23] B. M. Colosimo and M. Grasso, "Spatially weighted PCA for monitoring video image data with application to additive manufacturing," *J. Quality Technol.*, vol. 50, no. 4, pp. 391–417, Oct. 2018.
[24] J. Liu, C. Liu, Y. Bai, P. Rao, C. B. Williams, and Z. Kong, "Layer-wise spatial modeling of porosity in additive manufacturing," *IISE Trans.*, vol. 51, no. 2, pp. 109–123, Feb. 2019.
[25] S. Guo, W. G. Guo, and L. Bain, "Hierarchical spatial-temporal modeling and monitoring of melt pool evolution in laser-based additive manufacturing," *IISE Trans.*, vol. 52, no. 9, pp. 977–997, Sep. 2020.
[26] L.-E. Lindgren, A. Lundbäck, M. Fisk, R. Pederson, and J. Andersson, "Simulation of additive manufacturing using coupled constitutive and microstructure models," *Additive Manuf.*, vol. 12, pp. 144–158, Oct. 2016.
[27] J. C. Steuben, A. J. Birnbaum, J. G. Michopoulos, and A. P. Iliopoulos, "Enriched analytical solutions for additive manufacturing modeling and simulation," *Additive Manuf.*, vol. 25, pp. 437–447, Jan. 2019.
[28] W. L. Wang, C. M. Cheah, J. Y. H. Fuh, and L. Lu, "Influence of process parameters on stereolithography part shrinkage," *Mater. Des.*, vol. 17, no. 4, pp. 205–213, 1996.
[29] K. Tong, E. A. Lehtihet, and S. Joshi, "Parametric error modeling and software error compensation for rapid prototyping," *Rapid Prototyping J.*, vol. 9, no. 5, pp. 301–313, 2003.
[30] J. G. Zhou, D. Herscovici, and C. C. Chen, "Parametric process optimization to improve the accuracy of rapid prototyped stereolithography parts," *Int. J. Mach. Tools Manuf.*, vol. 40, no. 3, pp. 363–379, 2000.
[31] A. K. Sood, R. K. Ohdar, and S. S. Mahapatra, "Improving dimensional accuracy of fused deposition modelling processed part using grey Taguchi method," *Mater. Des.*, vol. 30, no. 10, pp. 4243–4252, 2009.
[32] J. Pan, Y. Zi, J. Chen, Z. Zhou, and B. Wang, "LiftingNet: A novel deep learning network with layerwise feature learning from noisy mechanical data for fault classification," *IEEE Trans. Ind. Electron.*, vol. 65, no. 6, pp. 4973–4982, Jun. 2018.
[33] C. Wang, X. P. Tan, S. B. Tor, and C. S. Lim, "Machine learning in additive manufacturing: State-of-the-art and perspectives," *Additive Manuf.*, vol. 36, Dec. 2020, Art. no. 101538.
[34] L. Cheng, K. Wang, and F. Tsung, "A hybrid transfer learning framework for in-plane freeform shape accuracy control in additive manufacturing," *IISE Trans.*, vol. 53, no. 2, pp. 298–312, 2020.
[35] R. Paul, S. Anand, and F. Gerner, "Effect of thermal deformation on part errors in metal powder based additive manufacturing processes," *J. Manuf. Sci. Eng.*, vol. 136, no. 3, Jun. 2014, Art. no. 031009.
[36] J.-M. Thiery, É. Guy, and T. Boubekeur, "Sphere-meshes: Shape approximation using spherical quadric error metrics," *ACM Trans. Graph.*, vol. 32, no. 6, pp. 1–12, Nov. 2013.
[37] S. N. Wood, *Generalized Additive Models: An Introduction With R*. Boca Raton, FL, USA: CRC Press, 2017.
[38] T. Hastie and R. Tibshirani, "Generalized additive models for medical research," *Stat. Methods Med. Res.*, vol. 4, no. 3, pp. 187–196, Sep. 1995.
[39] J. Cederbaum, M. Pouplier, P. Hoole, and S. Greven, "Functional linear mixed models for irregularly or sparsely sampled data," *Stat. Model.*, vol. 16, no. 1, pp. 67–88, Feb. 2016.
[40] K. W. De Bock, K. Coussement, and D. Van den Poel, "Ensemble classification based on generalized additive models," *Comput. Statist. Data Anal.*, vol. 54, no. 6, pp. 1535–1546, Jun. 2010.
[41] J. N. Goetz, R. H. Guthrie, and A. Brenning, "Integrating physical and empirical landslide susceptibility models using generalized additive models," *Geomorphology*, vol. 129, nos. 3–4, pp. 376–386, Jun. 2011.
[42] T. Hastie, R. Tibshirani, and J. Friedman, *The Elements of Statistical Learning: Data Mining, Inference, and Prediction*. New York, NY, USA: Springer, 2009.
[43] C. E. Rasmussen and C. K. I. Williams, *Gaussian Processes for Machine Learning*. Cambridge, MA, USA: MIT Press, 2006.
[44] X. Sun, P. L. Rosin, R. R. Martin, and F. C. Langbein, "Noise analysis and synthesis for 3D laser depth scanners," *Graph. Models*, vol. 71, no. 2, pp. 34–48, Mar. 2009.
[45] E. del Castillo, B. M. Colosimo, and S. D. Tajbakhsh, "Geodesic Gaussian processes for the parametric reconstruction of a free-form surface," *Technometrics*, vol. 57, no. 1, pp. 87–99, Jan. 2015.
[46] P. Bose, A. Maheshwari, C. Shu, and S. Wuhrer, "A survey of geodesic paths on 3D surfaces," *Comput. Geometry*, vol. 44, no. 9, pp. 486–498, Nov. 2011.
[47] O. Sorkine and M. Alexa, "As-rigid-as-possible surface modeling," in *Proc. Symp. Geometry Process.*, vol. 4, Jul. 2007, pp. 109–116.
[48] J. H. Friedman, "Stochastic gradient boosting," *Comput. Statist. Data Anal.*, vol. 38, no. 4, pp. 367–378, 2002.
[49] N. Decker, Y. Wang, and Q. Huang, "Efficiently registering scan point clouds of 3D printed parts for shape accuracy assessment and modeling," *J. Manuf. Syst.*, vol. 56, pp. 587–597, Jul. 2020.

Yuanxiang Wang (Member, IEEE) received the B.S. degree in finance from the East China University of Political Science and Law, Shanghai, China, in July 2015, and the M.S. degree in financial engineering and the Ph.D. degree in industrial and systems engineering from the University of Southern California, Los Angeles, CA, USA, in May 2017 and May 2022, respectively. His current research interests include domain-driven machine learning for advanced manufacturing and data science for engineering applications. He is a member of ASME and INFORMS. He has won the 2021 Bonder Foundation Award and the 2021 IEEE CASE Best Paper Award.

Cesar Ruiz received the Ph.D. degree in industrial engineering from the University of Arkansas in 2020. He is currently a Post-Doctoral Research Associate with the Daniel J. Epstein Department of Industrial and Systems Engineering, University of Southern California. His research concentrates on the effective use of domain knowledge for data science in engineering applications, such as manufacturing. He is a member of ASME, IISE, and INFORMS. He has won the 2019 MMR Best Conference Paper Award, the 2020 IISE QCRE William A. J. Golomski Award, and the 2021 IEEE CASE Best Paper Award.

Qiang Huang (Senior Member, IEEE) received the Ph.D. degree in industrial and operations engineering from the University of Michigan, Ann Arbor, MI, USA, in 2003. He is currently a Professor with the Daniel J. Epstein Department of Industrial and Systems Engineering, University of Southern California, Los Angeles, CA, USA. His recent research has been focusing on machine learning for additive manufacturing. He is an IISE Fellow. He was the Holder of the Gordon S. Marshall Early Career Chair in Engineering from 2012 to 2016. He has received the 2021 IEEE CASE Best Paper Award, the National Science Foundation (NSF) CAREER Award in 2011, and the IEEE TRANSACTIONS ON AUTOMATION SCIENCE AND ENGINEERING Best Paper Award from IEEE Robotics and Automation Society in 2014. He has served as an Associate Editor for IEEE TRANSACTIONS ON AUTOMATION SCIENCE AND ENGINEERING and IEEE ROBOTICS AND AUTOMATION LETTERS. He is a Department Editor for *IISE Transactions*. He is an Associate Editor for *ASME Transactions* and *Journal of Manufacturing Science and Engineering*.